

On-surface Synthesis of Mn-Phthalocyanines with optically active ligands

Amelia Domínguez-Celorio, Carlos Garcia-Fernandez, Sabela Quiroga, Peter Koval, Veronique Langlais, Diego Peña, Daniel Sánchez-Portal, David Serrate, and Jorge Lobo-Checa

This document contains:

- The Methods section with experimental and theory details.
- The ten supplementary figures referenced in the main text.
- Description of the precursor synthesis and corresponding spectroscopic data.
- The supplementary references.

S1. METHODS

Experimental details. Scanning tunneling microscopy experiments were performed using two ultrahigh vacuum low temperature scanning tunneling microscopes (an Omicron LT-STM and a Specs JT-STM) operating under 5K and with chamber pressures below 1×10^{-10} mbar.

The Ag(111) crystal was cleaned by repeated cycles of ionized argon sputtering (4×10^{-6} mbar, 1keV, 10mA, 20 minutes) and annealing (450°C, 15 minutes).

Manganese phthalocyanines were prepared directly on top of clean Ag(111) held at 50°C by simultaneous sublimation of precursor molecules and manganese in a 4:1 ratio onto the substrate at RT from a commercial electron-beam metal evaporator and a homemade Knudsen cell. Note that the singular deposition of **1a** in absence of Mn atoms yields extended compact islands structurally different from the ones shown in Fig. 2a. The MnPc's were obtained by post-annealing the samples for 30 minutes at 300°C for the cyclotetramerization into **3** and 350°C into **4**. A reduced efficiency of the cyclotetramerization reaction of **4** compared to **3** was evident from the subsequent STM images.

Theory details.

Periodic DFT calculations were performed using the Vienna *ab initio* package [1] within the spin-polarized generalized gradient approximation and the Perdew-Burke-Ernzerhof exchange correlation functional (GGA-PBE) [2]. We employed Projector augmented wave (PAW) pseudopotential from the VASP database [3] with a plane wave cutoff of 400 eV. The orbital occupancies were defined using a Methfessel-Paxton scheme with smearing width of $\sigma = 0.2$ eV. Self-consistent field convergence was considered sufficient for a total energy difference of less than 10^{-4} eV between iterations and the structures optimized until the atomic forces were smaller than 0.01 eV/Å.

The theoretical lattice constant of the cubic Ag bulk structure (neglecting dispersion interaction) was optimized to 4.146 Å, exceeding in 1.47% the experimental value of 4.085 Å. The corresponding Ag(111) surface was then modeled using a three-layer slab with a (9×10) surface unit cell, and a Γ -point centered $(3 \times 3 \times 1)$ Monkhorst-Pack mesh. Approximately 15 Å of vacuum was introduced along the surface normal direction to separate repeating slabs. During geometry optimization Van der Waals corrections were included through the zero damping DFT-D3 method

of Grimme [4]. In this framework, the adsorbed molecule and the top two Ag surface layers were permitted to fully relax, while the lowermost atomic layer was fixed at its bulk position.

S2. SUPPLEMENTARY FIGURES

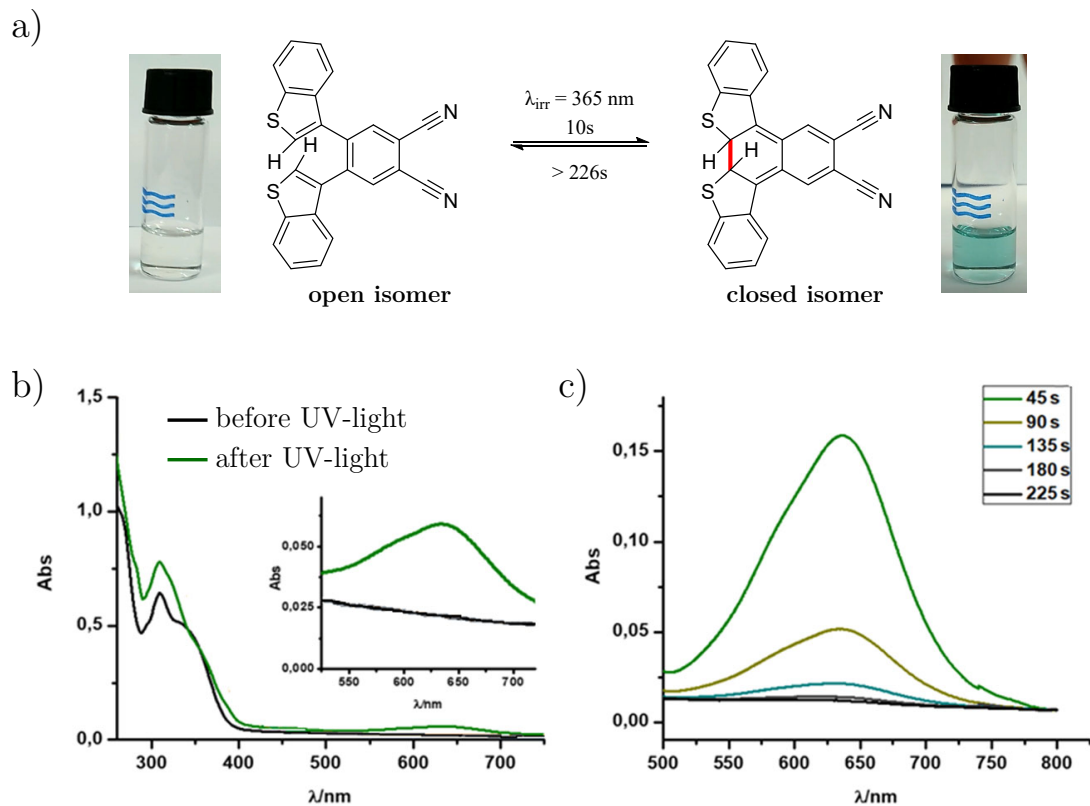


FIG. S1. Photochromic study of a solution of **1** in CHCl_3 a) Scheme of the reversible reaction of open and closed isomers and photographs of this solution taken before (left) and just after (right) irradiation with UV light ($\lambda = 365 \text{ nm}$). b) Corresponding visible UV absorption spectra before (black) and after (green) UV irradiation. c) Visible-UV absorption spectra at the region of interest recorded as a function of time.

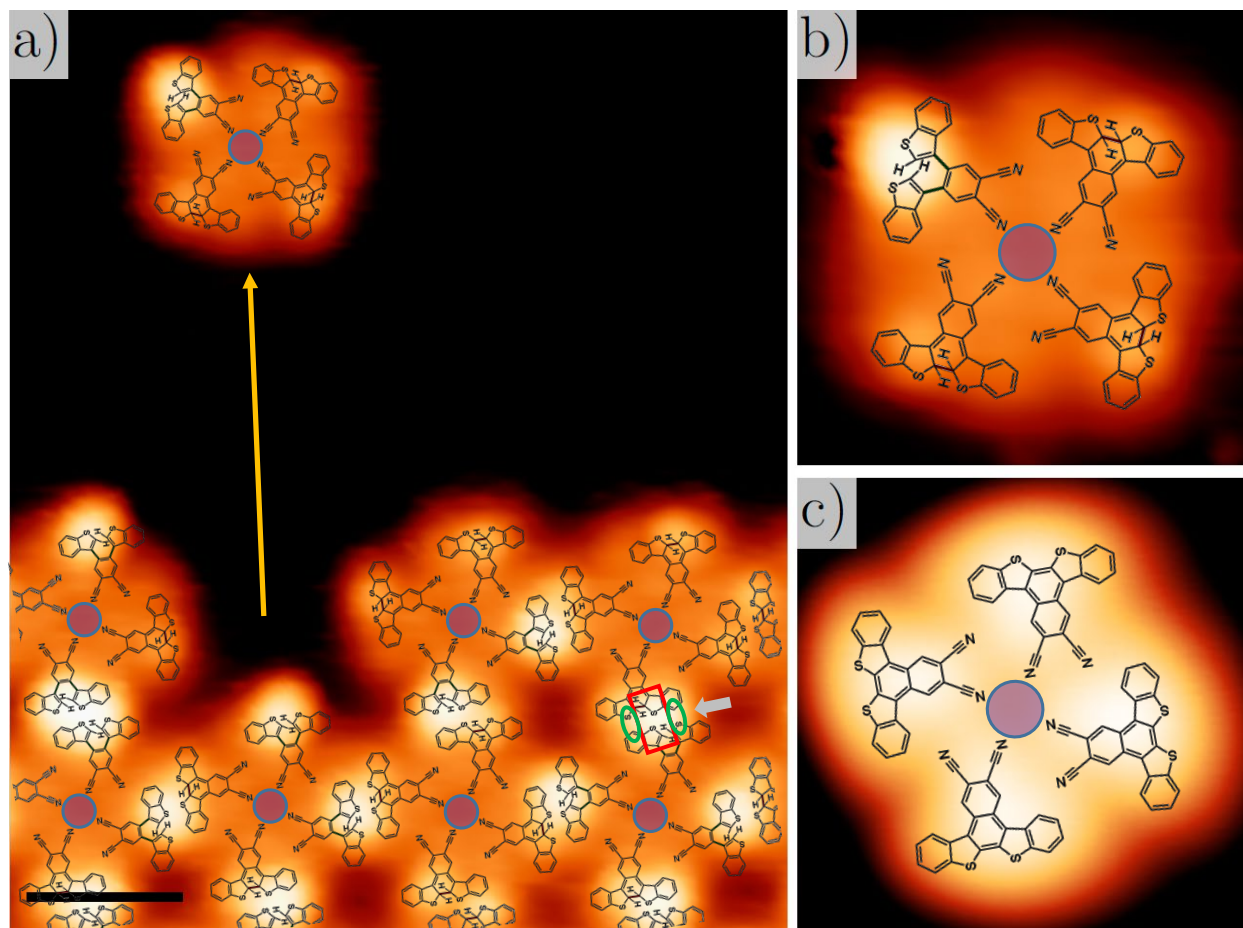


FIG. S2. Structural models of the metal-organic coordination units for the precursors **1** (a) and (b) and **2** (c) co-evaporated with Mn atoms (violet circles) on Ag(111). Both tetramers are stabilized through straight C-N···Mn bonds. These units are very stable and can be independently manipulated, as shown by the orange arrow in (a). Despite being practically identical to Mn + **1**, the tetramer units of Mn + **2** do not aggregate into islands, so the extra H atoms of **1a** must be responsible for such difference. We infer that the double direct H···S bonds marked by green ovals at the position of the grey arrow in (a) cannot provide by themselves the required stability due to the presence of the two adjacent repulsive S atoms (cf. red box) that prevent tetramer aggregation. However, the presence of the additional hydrogens in **1a** introduce slight vertical distortions that suffice to reduce this repulsion and steer the overall interaction to be dominated by the H···S bonds that result into tetramer aggregation. STM details: a) 2 nm scale bar, 0.6 V, 100 pA; b) and c) 3.5 x 3.5 nm², 0.6 V, 80 pA.

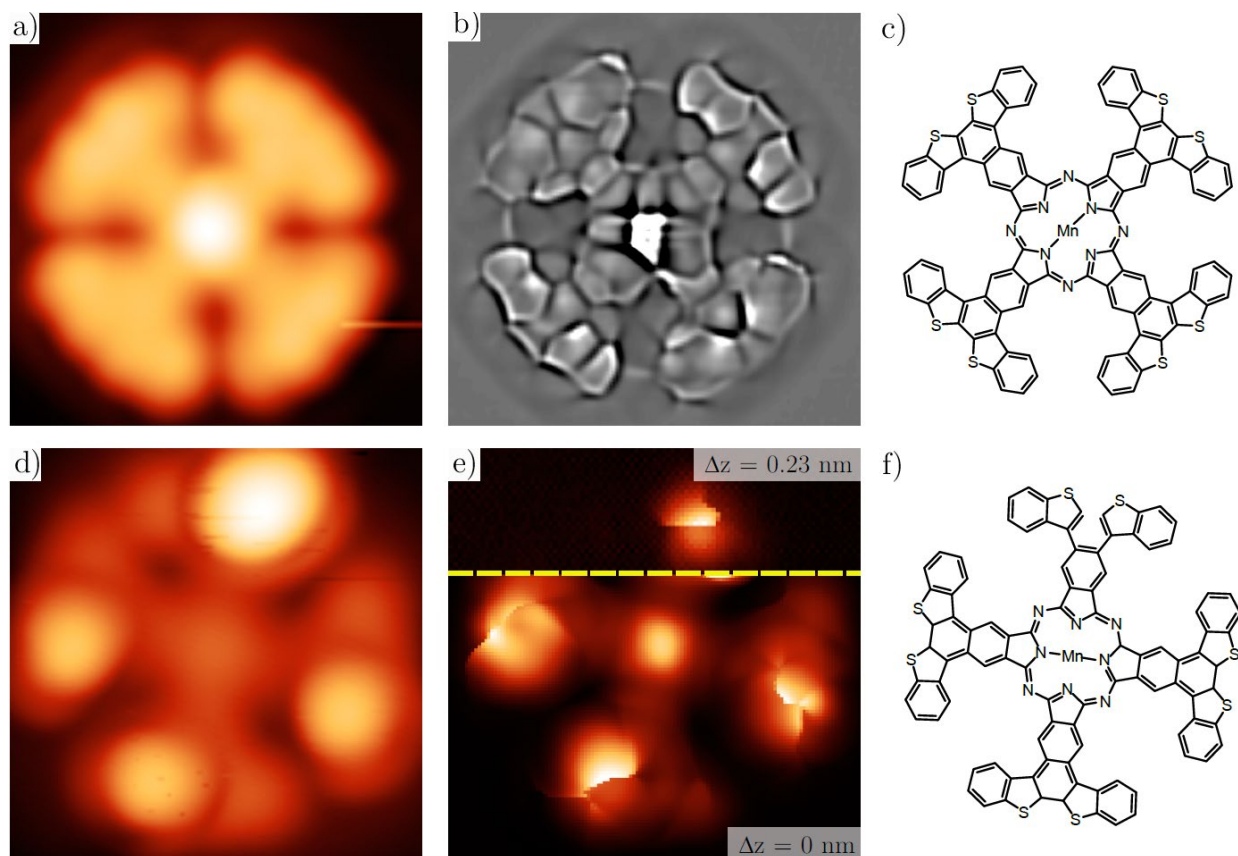


FIG. S3. Comparison between the quasi-planar structure of the fully conjugated MnPc (**4**, top row) and the switchable MnPc (**3**, bottom row) isomers. a) STM topography image of an individual molecule (0.5 V, 100 pA, $2.8 \times 2.8 \text{ nm}^2$). b) Laplace filtered bond resolved tunneling current image of such conjugated MnPc recorded at constant height with a CO-tip (3 mV, $2.8 \times 2.8 \text{ nm}^2$). c) Chemical structure of **4**. d) STM topography image of an individual molecule extracted from the island by atomic manipulation (0.4 V, 100 pA, $2.5 \times 2.5 \text{ nm}^2$). e) Tunneling current image recorded at constant height with a CO-tip vertically adjusting the tip height (3 mV, $2.5 \times 2.5 \text{ nm}^2$, with $\Delta z = +0.23 \text{ nm}$ above the yellow line). f) Chemical structure of **3**. Note that the cyclotetramerization reaction process of these MnPc's on the surface is corroborated by the visibility of the pyrrole ring and the slight distortion in a saddle shape of the four branches originating from **2**.

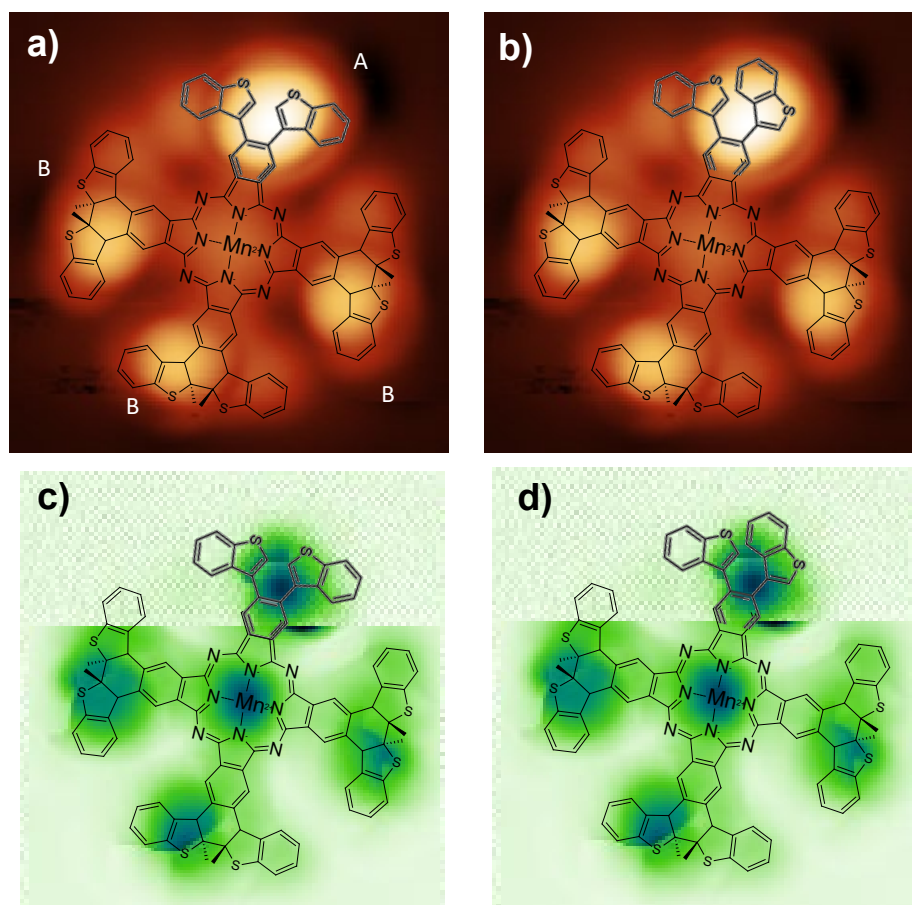


FIG. S4. Experimental comparison of the *open* and *open-rot* configurations using constant current (top image) and constant height imaging (bottom image) taken from panels d) and e) in Fig.S3. The model must fit simultaneously both images. We find that the *open* configuration in a) and c) fits better both datasets. Contrarily, the external benzene ring of the *open-rot* case that should be dominant, since it is the one pointing away furthest from the surface, is practically featureless in comparison. a) and b) STM topography image (constant current, 0.4 V, 100 pA, $2.5 \times 2.5 \text{ nm}^2$); c) and d) Tunneling current image recorded at constant height with a CO-tip vertically adjusting the tip height (3 mV, $2.5 \times 2.5 \text{ nm}^2$, with $\Delta z = +0.23 \text{ nm}$ at the top).

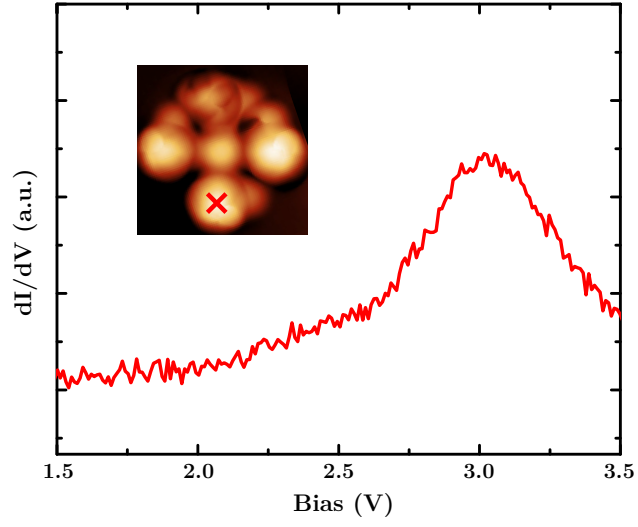


FIG. S5. Conductance spectrum recorded with closed feedback on the A-branch of a **(3)** isomeric MnPc as the one shown in the STM image inset (-50 mV, 20 pA). Note that the spectrum is featureless until it peaks at 3.1 V. STS parameters: $V_{mod} = 10$ mV, set point 1 V, 100 pA.

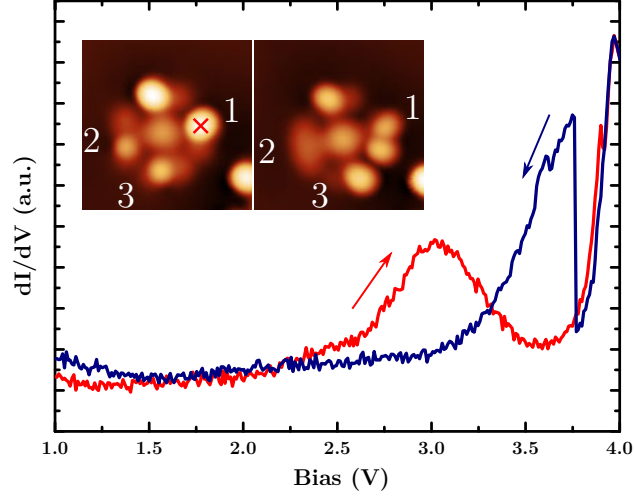


FIG. S6. STM topography images recorded before (left) and after (right) the bias ramp at the marked position by the red cross (-50 mV, 20 pA, 4×4 nm²). The graph shows the evolution of the conductance in closed feedback mode as a function of the bias (up-ramp in red, down-ramp in blue). A jump in the down-ramp spectrum occurs at 3.7 V, which is a manifestation of the structural change observed in the branches (1) and (2) when ramping in the positive bias range. The apparent shape and electronic structure of the modified branches do not correspond neither to *open* nor to *trans-closed* configurations. The bottom branch (3) changes from *trans-closed* to *open* configuration, attributable to an electric field driven switch. Notably, ramping in negative biases did not produce switching in any of the branches.

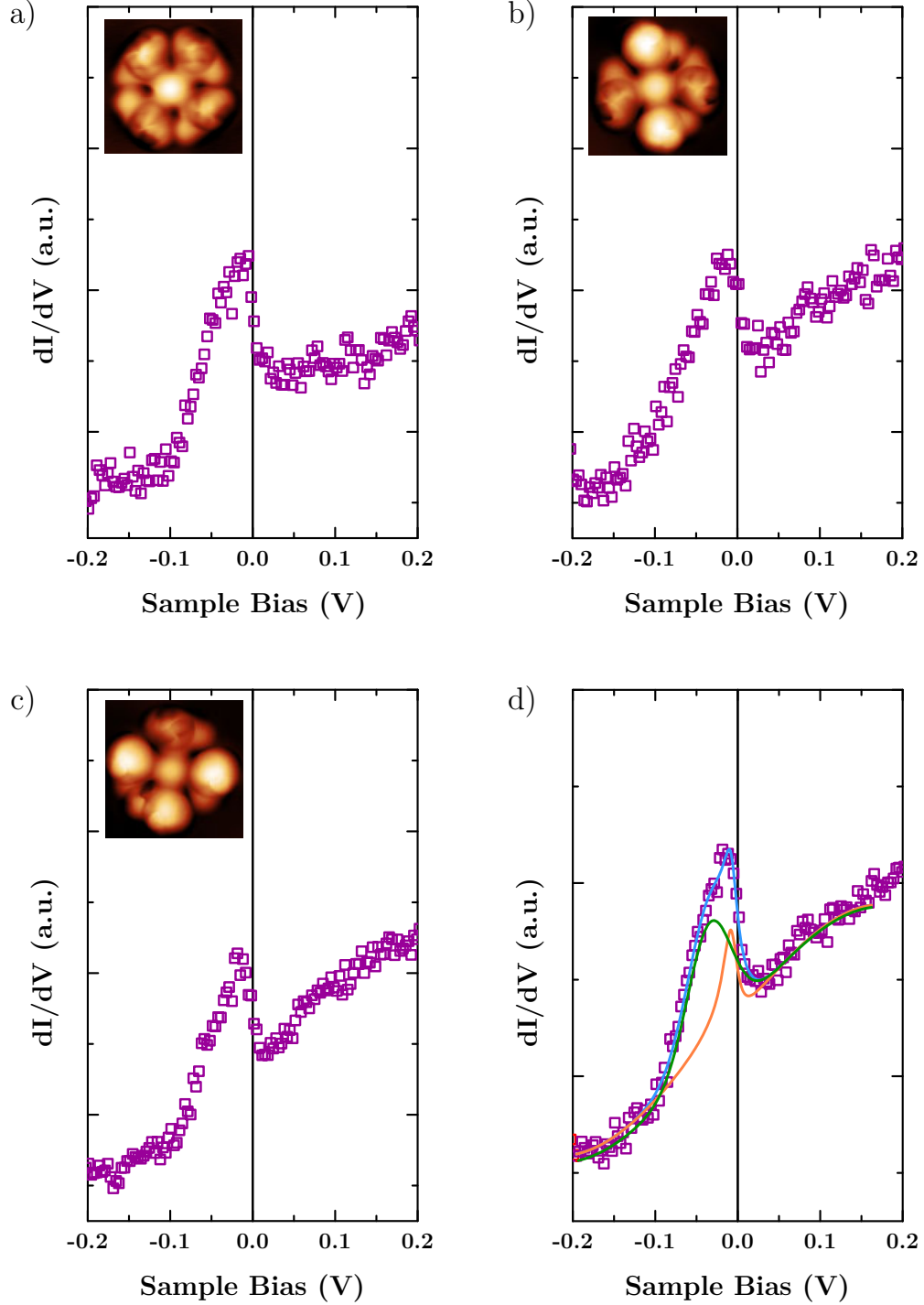


FIG. S7. a)-c) Differential conductance (dI/dV) spectra recorded on the central manganese ions of selected MnPc's with different branches configurations (cf. insets) ($V_{mod} = 1$ mV, set point: -1 V, 20 pA). d) Similarly to the analysis in supplemental references [5] and [6], averaged dI/dV spectra recorded on Mn ions a)-c) (violet) were fitted to a function (blue) composed by a Fano (orange) and a Gaussian (green) function representing the Kondo resonance and the d -orbital state respectively.

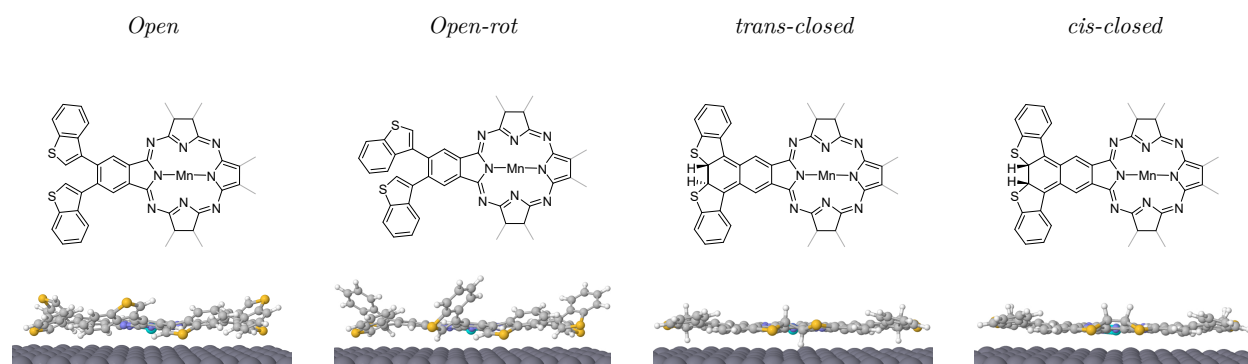


FIG. S8. Chemical models of the corresponding branch configurations and the DFT calculated sideviews on a Ag(111) substrate (with the back branch removed for visualization purposes). A fourth conformation, the *cis-closed* configuration (depicted at the right), was identified and immediately discarded due to the experimental absence of fully symmetric branches.

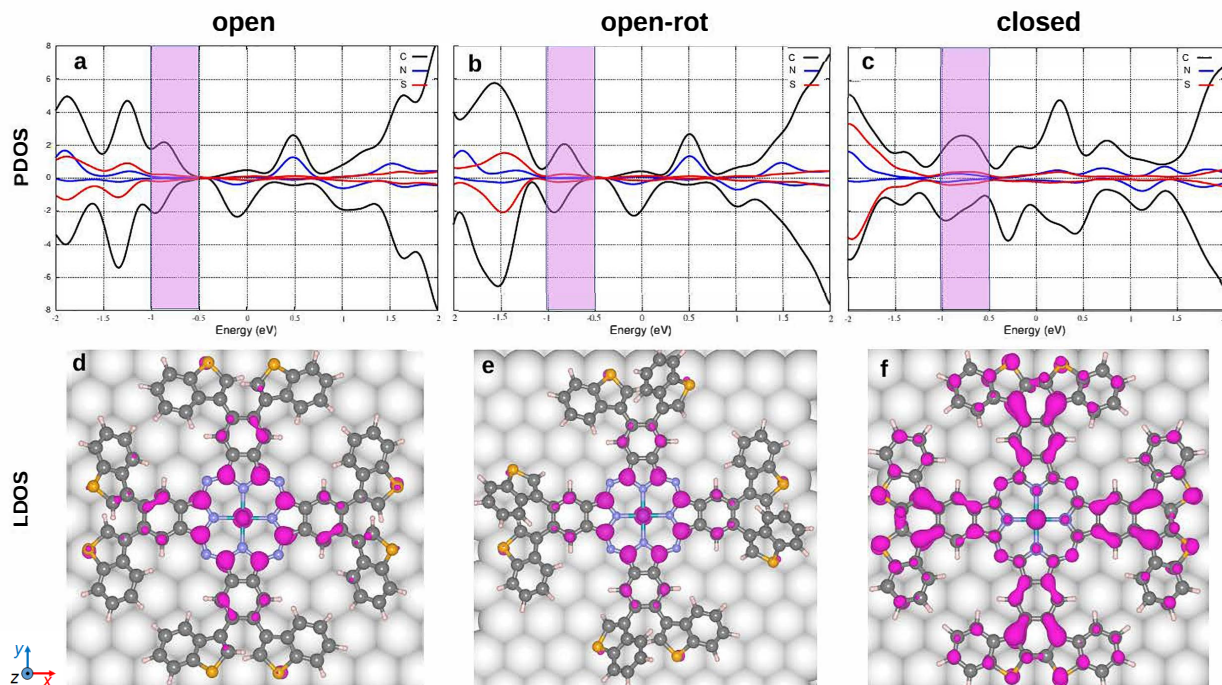


FIG. S9. Projected density of states (PDOS) calculated from DFT onto C (black), N (blue) and S (red) orbitals for isomeric MnPc with four *open* (a), four *open-rot* (b) and four *trans-closed* (c) branches adsorbed on Ag(111) surface. Local density of states for the highest fully occupied molecular orbital in the energy window $[-1, -0.5]$ eV for **3** with the four branches in *open* (d), *open-rot* (e) and *trans-closed* configurations (f). In this energy range, the electronic density delocalize over the external branches on the *trans-closed* while it remains at the pyrrole ring center in the *open* /*open-rot* configurations. Thus, we correlate the *trans-closed* molecular orbital depicted in (f) with the experimental dI/dV feature observed at $-1, 3$ V Fig 4(c). Images of the singly occupied molecular orbital near the Fermi level (0 eV) qualitative agree with the features shown by the LDOS picture in the energy range $[-1, -0.5]$ eV. A broader DOS distribution around the Fermi level is attributed to a strong interaction of the *trans-closed* molecule with the Ag surface. Furthermore, a shift to lower energies in the HOMO position is appreciated for the *open* /*open-rot* structures due to the lower conjugation of its branches with the pyrrole ring center.

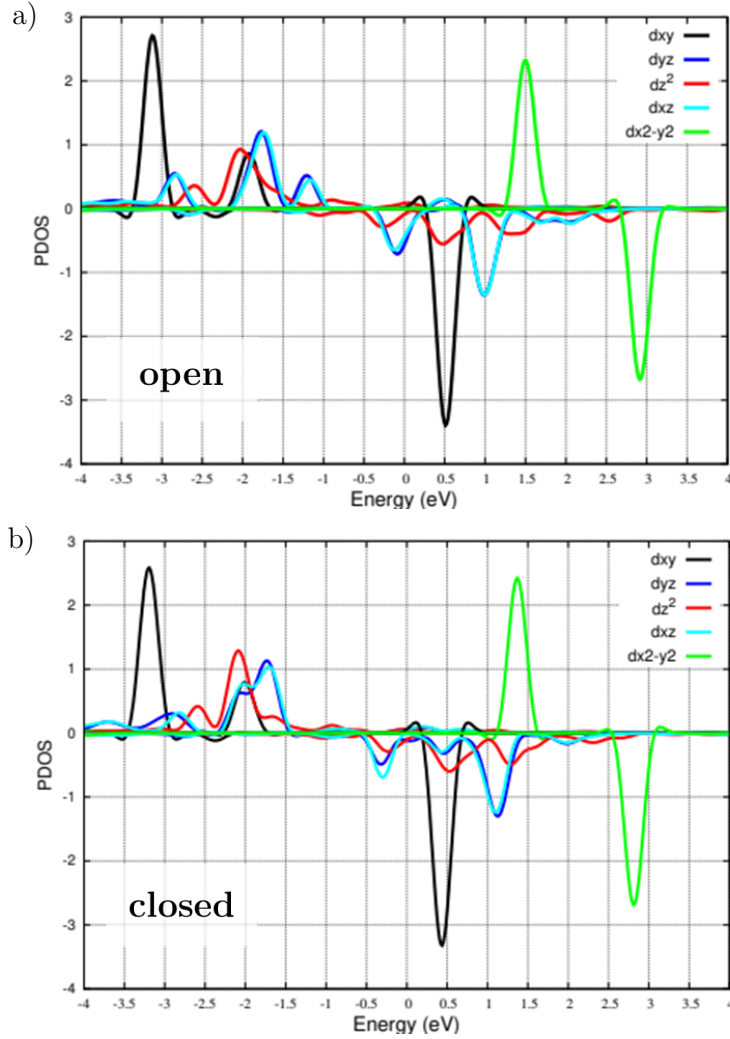


FIG. S10. Projected density of states (PDOS) calculated from DFT onto Mn d orbitals for isomeric MnPc with four *open* (a) and four *trans-closed* (b) branches adsorbed on Ag(111) surface. The Fermi level is set to the zero value in the bottom axis. Open and closed configurations do not show any significant difference of their magnetic properties. As depicted, the $d_{x^2-y^2}$ orbital is empty, whereas the other four d -orbitals are filled for the up channel. The spin down component shows partial occupation in the double degenerated d_{xz}, d_{yz} and the d_{z^2} resulting in a total magnetic moment of approximately $3 \mu_B$. Comparison with the gas phase calculation show a similar partial occupations for the d_{xz}, d_{yz} orbital and therefore can be assigned to the coordination of the Mn center with the molecular framework. The main observed difference with respect to the gas phase calculation was related to the broadening of the d_{z^2} down component, allowing a partial occupation of this orbital instead of a well defined empty state. This effect associated to a strong interaction with the Ag surface is in agreement with previous work [5, 6] where the d_{z^2} orbital was identified to play a key role in the origin of the Kondo resonance. The computed total magnetic moment for the molecule + surface system was approximately $2 \mu_B$ due to an opposite magnetic contribution of the molecular framework.

S3. DESCRIPTION OF THE PRECURSOR SYNTHESIS AND CORRESPONDING SPECTROSCOPIC DATA

A. General methods

All reactions were carried out under argon using oven-dried glassware. TLC was performed on Merck silica gel 60 F254; chromatograms were visualized with UV light (254 and 360 nm). Flash column chromatography was performed on Merck silica gel 60 (ASTM 230-400 mesh). ^1H and ^{13}C NMR spectra were recorded at 300 and 75 MHz (Varian Mercury 300 instrument). High-resolution spectra APCI were obtained on a Bruker Microtof. UV/Vis spectra were obtained on a Jasco V-530 spectrophotometer.

Commercial reagents and anhydrous solvents were purchased from ABCR GmbH, Aldrich Chemical Co., or Strem Chemicals Inc., and were used without further purification.

B. Experimental details and spectroscopic data

Synthesis of 4,5-bis(benzo[b]thiophen-3-yl)phthalonitrile (1a).

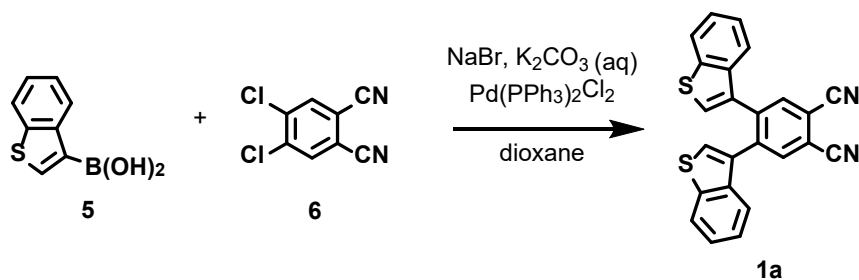


FIG. S11. Synthesis pathway of **1a**.

Fig. S11: A mixture of the boronic acid **5** (50 mg, 0.25 mmol), 4,5-dichlorophthalonitrile (**6**, 280 mg, 1.02 mmol), NaBr (26 mg, 0.25 mmol) and a saturated aqueous solution of K₂CO₃ (141 mg, 1.02 mmol) in 1,4-dioxane (13 mL) were refluxed under argon. After 5 min Pd(PPh₃)Cl₂ (3.5 mg, 0.005 mmol) was added and the mixture was refluxed for 16 h. Then, the solvent was evaporated under reduced pressure and the residue was purified by column chromatography (SiO₂; hexane/AcOEt/CH₂Cl₂ (8.5:0.5:1)) to isolate compound **1a** (72 mg, 74%) as a white solid (m.p.: 201-204°C).

$^1\text{H NMR}$ (298 K, 300 MHz, CDCl_3) δ : 8.06 (s, $J = 1.3$ Hz, 2H), 7.77 (d, $J = 7.5$ Hz, 2H), 7.46 (dd, $J = 7.2, 0.9$ Hz, 2H), 7.36 – 7.19 (m, $J = 14.9, 7.2, 1.2$ Hz, 4H), 7.15 (s, $J = 2.9$ Hz, 2H) ppm. $^{13}\text{C NMR}$ (298 K, 75 MHz, CDCl_3) δ : 141.01 (2C), 139.81 (2C), 136.91 (2C), 135.92 (2CH), 132.72 (2C), 127.36 (2CH), 124.95 (2CH), 124.90 (2CH), 122.92 (2CH), 121.68 (2CH), 115.33 (2C), 114.70 (2C) ppm. **EM (APCI (M+1)) high resolution** for $\text{C}_{24}\text{H}_{13}\text{N}_2\text{S}_2$, calculated: 393.5089, experimental: 393.5088. **UV/Vis** (CH_2Cl_2) λ_{max} : 305, 325 nm.

Synthesis of dicyanonaphthalene (2).

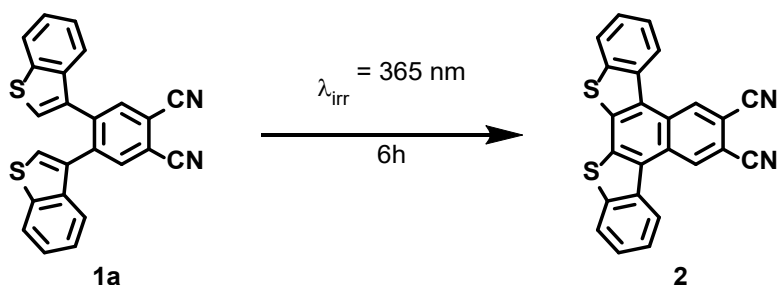


FIG. S12. Synthesis pathway of **2**.

Fig. S12: A solution of phthalonitrile **1a** (10 mg, 0.026 mmol) in CH_2Cl_2 (3 mL) was irradiated with $\lambda_{\text{irr}} = 365$ nm for 6h. The resulting precipitate was centrifuged to yield dicyanonaphthalene **2** as a yellow solid (10 mg, 100%).

$^1\text{H NMR}$ (353 K, 300 MHz, $\text{C}_2\text{D}_2\text{Cl}_4$) δ : 9.54 (s, 2H), 8.73 (d, $J = 8.1$ Hz, 2H), 8.08 (d, $J = 8.0$ Hz, 2H), 7.67 (m, 4H) ppm. Due to the low solubility of **2**, it was not possible to obtain the $^{13}\text{C NMR}$ spectrum. **EM (APCI (M+1)) high resolution** for $\text{C}_{24}\text{H}_{11}\text{N}_2\text{S}_2$, calculated: 391.0358, experimental: 391.0361. **UV/Vis** (CH_2Cl_2) λ_{max} : 290, 325 nm.

C. ^1H and ^{13}C NMR spectra

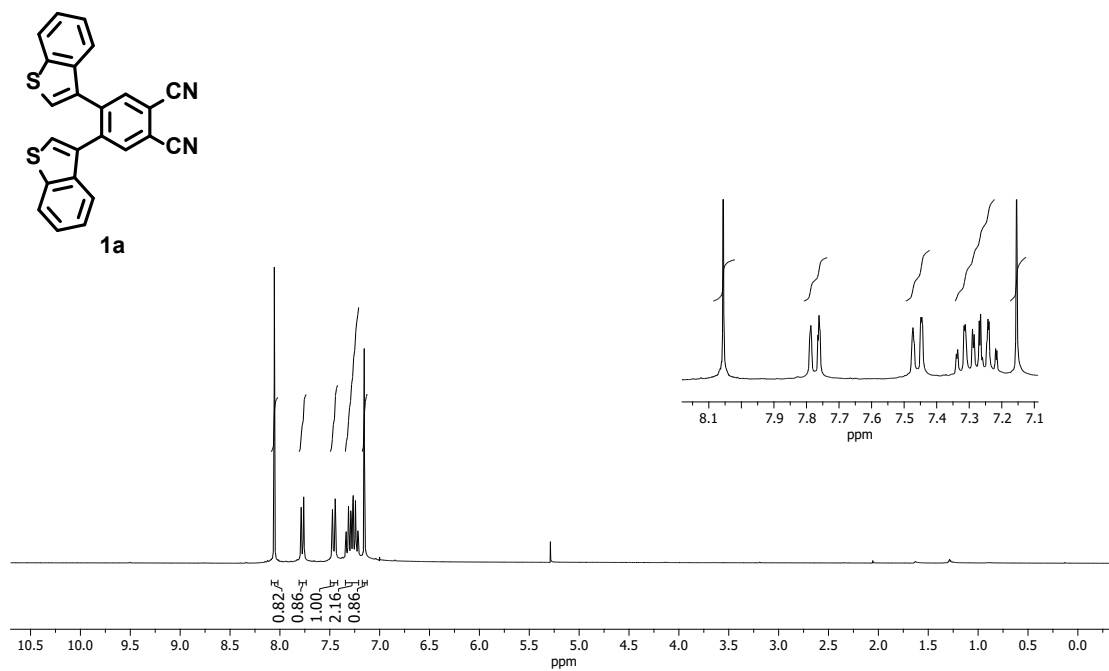


FIG. S13. ^1H NMR spectrum of compound **1a**.

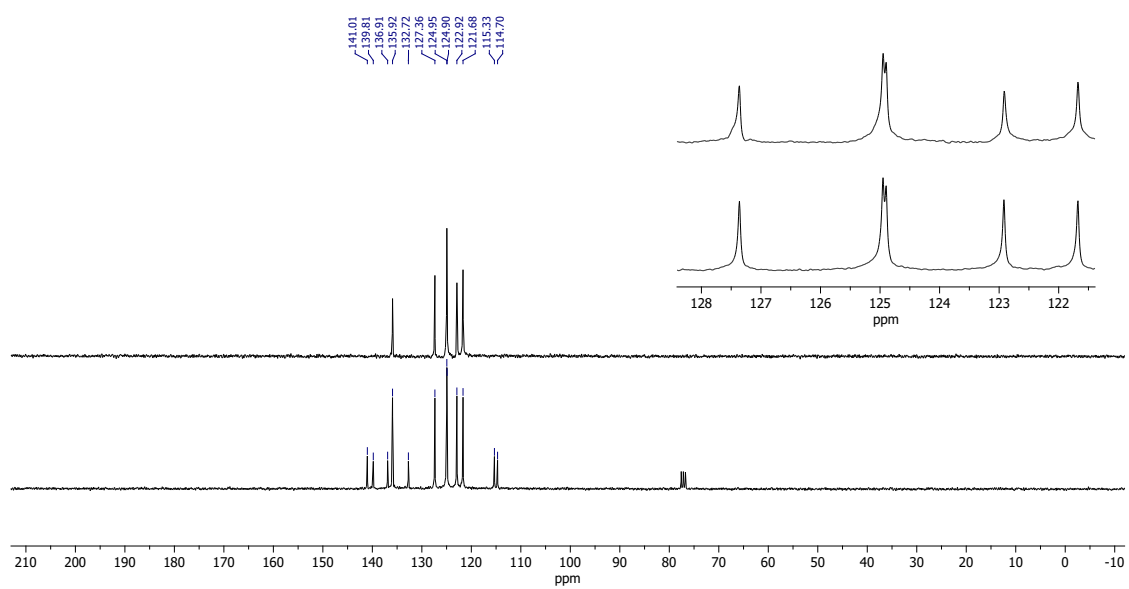


FIG. S14. ¹³C NMR spectrum of compound **1a**.

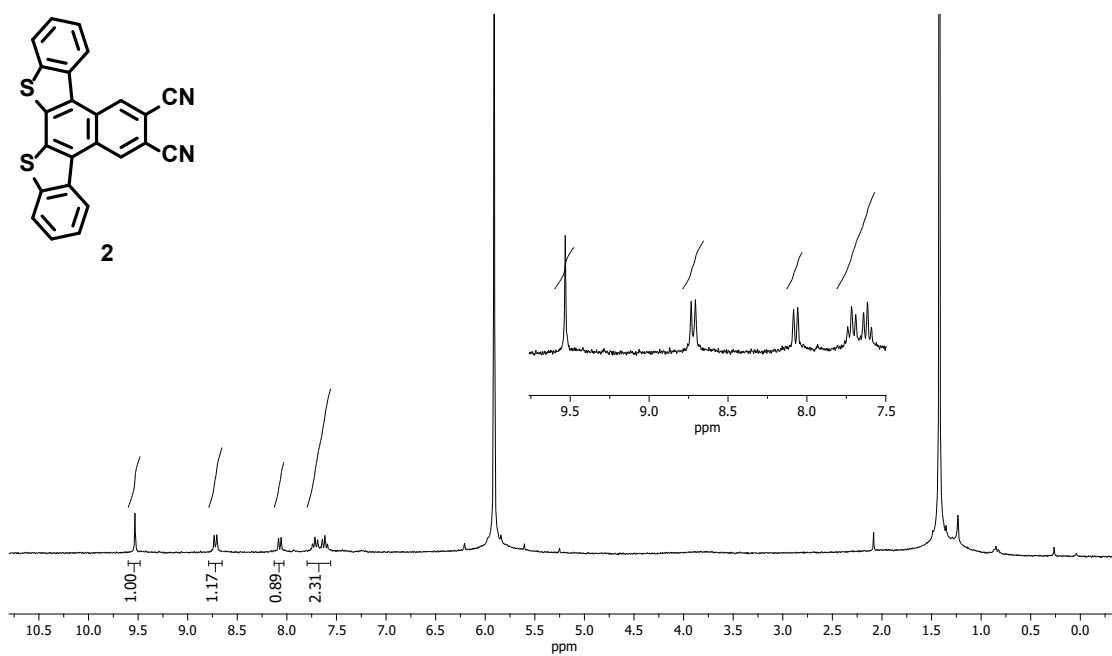


FIG. S15. ¹H NMR spectrum of compound **2**.

-
- [1] G. Kresse and J. Furthmüller., *Comput. Mat. Sci.* p. 6:15 (1996).
- [2] J. P. Perdew, K. Burke, and M. Ernzerhof, *Phys. Rev. Lett.* **78**, 1396 (1997), URL <http://link.aps.org/doi/10.1103/PhysRevLett.78.1396>.
- [3] G. Kresse and D. Joubert, *Phys. Rev. B* **59**, 1758 (1999), URL <https://link.aps.org/doi/10.1103/PhysRevB.59.1758>.
- [4] S. Grimme, S. Ehrlich, and L. Goerigk, *Journal of Computational Chemistry* **32**, 1456 (2011), <https://onlinelibrary.wiley.com/doi/pdf/10.1002/jcc.21759>, URL <https://onlinelibrary.wiley.com/doi/abs/10.1002/jcc.21759>.
- [5] J. Kügel, M. Karolak, J. Senkpiel, P.-J. Hsu, G. Sangiovanni, and M. Bode, *Nano Letters* **14**, 3895 (2014).
- [6] R. Tuerhong, F. Ngassam, S. Watanabe, J. Onoe, M. Alouani, and J.-P. Bucher, *The Journal of Physical Chemistry C* **122**, 20046 (2018).